



Defence Research and
Development Canada

Recherche et développement
pour la défense Canada

Copy No:



Report on the effect of ambient pressure on laser spark characteristics

Jason Etele

Prepared by:

The Aldanox Group, Inc.

5474 Edgewater Drive, Manotick, Ontario, Canada, K4M-1B4

Contract Project Manager: Dr. Jason Etele, 613-327-3816

Contract Number: W7701-4500907304

Contract Scientific Authority: Dr. Rogerio Pimentel, 418-844-4000 x 4170

The scientific or technical validity of this Contract Report is entirely the responsibility of the Contractor and the contents do not necessarily have the approval or endorsement of Defence R&D Canada.

Defence R&D Canada – Valcartier

Contract Report
DRDC Valcartier CR 2012-066
March 2012

Canada 

Report on the effect of ambient pressure on laser spark characteristics

Jason Etele

Prepared by:
The Aldanox Group, Inc.
5474 Edgewater Drive
Manotick, Ontario, Canada, K4M 1B4

Contract Project Manager: Dr. Jason Etele, 613-327-3816
Contract Number: W7701-4500900374
Contract Scientific Authority: Dr. Rogerio Pimentel, 418-844-4000 Ext. 4170

The scientific or technical validity of this Contract Report is entirely the responsibility of the Contractor and the contents do not necessarily have the approval or endorsement of Defence R&D Canada.

Defence R&D Canada – Valcartier
Contract Report
DRDC Valcartier CR 2012-066
March 2012

Approved by

Original signed by Rogerio Pimentel

Rogerio Pimentel

Contract Scientific Authority, Defence R & D Canada - Valcartier

Approved for release by

Original signed by Marc Lauzon

Marc Lauzon

Section Head, Precision Weapons Section, Defence R & D Canada - Valcartier

© Her Majesty the Queen in Right of Canada, as represented by the Minister of National Defence, 2012

© Sa Majesté la Reine (en droit du Canada), telle que représentée par le ministre de la Défense nationale, 2012

Table of contents

Table of contents	i
List of figures	ii
1 Introduction	1
2 Governing Equations	2
3 Results	8
4 Conclusions and Recommendations	14
References	15
List of Acronyms and Symbols	16

List of figures

Figure 1:	Image of emission from Glumac et al. [1] at 25 ns	8
Figure 2:	Initial conditions	9
Figure 3:	Temperature contours at approximately 170 μ s for three domain sizes . .	9
Figure 4:	Temperature contours at approximately 460 μ s for three domain sizes . .	10
Figure 5:	Streamline pattern at 170 μ s obtained in the medium size domain	10
Figure 6:	Comparison of temperature contours for different grid sizes in the medium sized domain	11
Figure 7:	Maximum temperature	12
Figure 8:	Comparison of temperature contours at 1 and 0.5 atm in the medium domain using the fine grid	13

1 Introduction

The creation of plasma regions in high-speed flows for flow control purposes is a strategy being pursued by numerous research organizations. Laser-induced plasmas have significant potential due to their fast response times and ability to produce flow perturbations at extended distances. Most studies applying laser sparks in air have investigated the characteristics of laser-induced plasmas near atmospheric pressure at sea level. However, for many aerospace applications the static pressures involved are significantly smaller. In particular, for high-speed applications the flight regimes involve altitudes where pressures can be as small as 0.1 atm. This has motivated experimental investigation into the effect of ambient pressure on laser spark characteristics. These results can be used to validate numerical methods seeking to simulate this process.

Work done by Glumac and Elliot [1] and Glumac et al.[2] experimentally investigate the generation of a small region of plasma in air initially at atmospheric pressure and temperature. Light intensity images are obtained over approximately 1000 μs to determine the shape and behaviour of the plasma region. The plasma is generated using a solid state 180 mJ Nd:YAG (neodymium-doped yttrium aluminium garnet) laser with a 532 nm wavelength. A spark is generated using a 7 ns pulse passed through a lens to a focal point within a small chamber in which the ambient pressure can be controlled. The effect of varying atmospheric pressure is investigated to determine the implications of reduced pressures (below atmospheric) on the temporal temperature profile of the plasma and the fraction of laser energy absorbed by the fluid. Pressures from 1 atm down to 0.1 atm are investigated.

The report contains a summary of numerical results obtained using an axisymmetric code originally based on the simulation of a laser sustained plasma in Argon. The governing equations are presented with several modifications to accommodate the difference between Argon and air (modelled here as pure Nitrogen). Recommendations are included with regards to improving the numerical approach so that increased accuracy with respect to the experimental results can be obtained.

2 Governing Equations

Although often considered a fourth state of matter, plasmas behave in many respects as fluids and thus can be approximated using the traditional Navier-Stokes equations. However, the electromagnetic properties of plasmas require some modification to these equations in order to properly account for the various degrees of ionization possible, as well as the additional energy storage and transfer mechanisms that exist. This approach is advantageous in cases where the plasma is generated from a neutral gas as then both states can be solved using a single approach. Therefore, this is the approach taken where in two dimensional or axisymmetric (cylindrical) co-ordinates the single species, laminar, non-reacting, Navier-Stokes equations can be expressed as,

$$\frac{\partial Q}{\partial t} + \frac{\partial F}{\partial x} + \frac{\partial G}{\partial r} + S_{axi} - \frac{\partial F_v}{\partial x} - \frac{\partial G_v}{\partial r} - S_{axi_v} = Z \quad (1)$$

where the solution vector Q and the convective vectors can be expressed as,

$$Q = \begin{bmatrix} \rho_n \\ \rho_p \\ \rho u \\ \rho v \\ E \end{bmatrix} \quad F = \begin{bmatrix} \rho_n u \\ \rho_p u \\ \rho u^2 + p \\ \rho uv \\ u(E + p) \end{bmatrix} \quad G = \begin{bmatrix} \rho_n v \\ \rho_p v \\ \rho uv \\ \rho v^2 + p \\ v(E + p) \end{bmatrix} \quad (2)$$

The total density is simply the sum of both the neutral particle and charged (positive) particle densities ($\rho = \rho_n + \rho_p$) when the mass of the electrons is considered negligible. For a single species gas or plasma, diffusion terms can be removed allowing the viscous terms to be expressed as,

$$F_v = \begin{bmatrix} 0 \\ 0 \\ \tau_{xx} \\ \tau_{xr} \\ \kappa \frac{\partial T}{\partial x} + \tau_{xx}u + \tau_{xr}v \end{bmatrix} \quad G_v = \begin{bmatrix} 0 \\ 0 \\ \tau_{rx} \\ \tau_{rr} \\ \kappa \frac{\partial T}{\partial r} + \tau_{rx}u + \tau_{rr}v \end{bmatrix} \quad (3)$$

and the terms unique to an axisymmetric simulation can be expressed as,

$$S = \frac{1}{r} \begin{bmatrix} \rho_n v \\ \rho_p v \\ \rho uv \\ \rho v^2 + p \\ v(E + p) \end{bmatrix} \quad S_{axi_v} = \frac{1}{r} \begin{bmatrix} 0 \\ 0 \\ \tau_{rx} \\ \tau_{rr} - \tau_{\theta\theta} \\ \kappa \frac{\partial T}{\partial r} + \tau_{rx}u + \tau_{rr}v \end{bmatrix} \quad (4)$$

The equations expressed by Eq. 1 are solved using a cell centred finite volume scheme where the inviscid fluxes F and G are approximated using the advection upstream splitting method (AUSM-DV) with accuracy extended to third order using MUSCL and a pressure limiter. Viscous terms are treated using central differences while the lower/upper symmetric Gauss-Seidel line relaxation scheme extended to third order accuracy by Matsuno's inner iteration method is used for the time integration.

From Dalton's law of partial pressures and the perfect gas equation of state, if one assumes a neutral plasma where the density of positive and negative ions is equal then the plasma pressure can be expressed as,

$$p = \sum_k p_k = \sum_k \rho_k R_k T = (\rho_n + 2\rho_p)RT \quad (5)$$

The shear stresses, both normal and tangential to the planes under consideration, can be derived from the mechanics of Newtonian fluids and expressed as functions of the flow properties. In the case of axisymmetric flow these stresses can be written in cylindrical co-ordinates using Stokes' hypothesis as,

$$\tau_{rx} = \tau_{xr} = \mu \left(\frac{\partial v}{\partial x} + \frac{\partial u}{\partial r} \right) \quad (6)$$

$$\tau_{xx} = \mu \left\{ \frac{4}{3} \frac{\partial u}{\partial x} - \frac{2}{3} \frac{\partial v}{\partial r} - \frac{2}{3} \frac{v}{r} \right\} \quad (7)$$

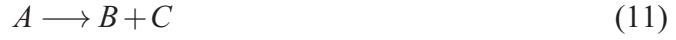
$$\tau_{rr} = \mu \left\{ -\frac{2}{3} \frac{\partial u}{\partial x} + \frac{4}{3} \frac{\partial v}{\partial r} - \frac{2}{3} \frac{v}{r} \right\} \quad (8)$$

$$\tau_{\theta\theta} = \mu \left\{ -\frac{2}{3} \left(\frac{\partial u}{\partial x} + \frac{\partial v}{\partial r} \right) + \frac{4}{3} \frac{v}{r} \right\} \quad (9)$$

The vector Z contains the terms specific to the plasma nature of the flow. Each of the species equations contains a source term to reflect the ionization/recombination processes occurring while the energy equation contains terms which account for the absorption of laser energy into the flow field. In the current formulation this electromagnetic source vector is,

$$Z = \begin{bmatrix} -\omega_f \rho_p \rho_n + \omega_b \rho_p^3 \\ \omega_f \rho_p \rho_n - \omega_b \rho_p^3 \\ 0 \\ 0 \\ q \end{bmatrix} \quad (10)$$

Assuming thermal equilibrium the ionization and recombination reactions can be found using Saha's equation. If the following chemical reaction is assumed,



then Saha's equation can be written as

$$\frac{n_B n_C}{n_A} = \left(\frac{2\pi k_B T m_B m_C / m_A}{h_p^2} \right)^{3/2} \frac{Z_B Z_C}{Z_A} \quad (12)$$

Where Z_A , Z_B and Z_C are the internal partition functions of the elements A, B and C respectively. The internal partition function is a summation over all possible energy levels ϵ_i , with a degeneracy of w_i and has the following form:

$$Z_A = \sum_i w_i e^{-\epsilon_i / k_B T} \quad (13)$$

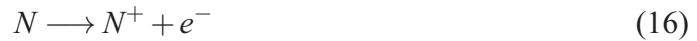
As energy is absorbed in air (modelled as pure N_2) there are two possible reactions. The first is the dissociation of diatomic Nitrogen into two single Nitrogen molecules,



The second is the direct ionization of diatomic Nitrogen to produce N_2^+ :



With significant quantities of atomic Nitrogen present the process of ionization will follow the reaction,



According to Wang [3] N_2^+ is not present in significant quantities because the dissociation reaction requires less energy than the ionization reaction. Therefore, below $\sim 10,000$ K) it is mostly molecular Nitrogen which exists, while at higher temperatures with almost all of the N_2 dissociated the reaction in Eq. 15 does occur in significant quantities. For the current results the code is limited to a single species and thus only monatomic Nitrogen is modelled. To calculate the ionization of this species the partition function is approximated by,

$$\frac{Z_N^+}{Z_N} = e^{-\varepsilon_i/k_B T} = e^{-1.68 \times 10^5 / T} \quad (17)$$

which can then be used in the Saha equation for this reaction,

$$\frac{n_N^+ n_e}{n_N} = \left(\frac{2\pi k_B T m_e}{h_p^2} \right)^{3/2} \frac{2Z_N^+}{Z_N} \quad (18)$$

Going back to Eq 10, the forward reaction rate in the species source terms can be expressed as,

$$\omega_f = \frac{1.15 \times 10^{27}}{T^3} e^{-\varepsilon_i/k_B T} \quad (19)$$

With this value, along with the ratio of ions to neutral particles of Nitrogen from Eq. 18 one can calculate the backwards recombination rate using,

$$\omega_b = \frac{1}{M} \frac{n_N}{n_N^+ n_e} \omega_f \quad (20)$$

With the terms particular to a plasma incorporated into the species continuity equations, one must consider the effects of the plasma on the energy equation (for the cases considered here there are no externally applied electric or magnetic fields and thus there are no additional forces which need be added to the momentum equations). Both plasmas and neutral gases contain internal and kinetic energies. However, if a portion of the flow is ionized then the energy required for this ionization must be considered. Adding this to the energy term in Eq. 2 yields,

$$E = \frac{p}{\gamma - 1} + \frac{1}{2} \rho (u^2 + v^2) + \rho_p H_p \quad (21)$$

where the enthalpy of the plasma, H_p , is taken as equal to the ionization energy,

$$H_p = \varepsilon_i / MW_n \quad (22)$$

To calculate the energy absorbed by the gas from the laser, the average absorption rate inside a cell with a width Δx along a single ray n into which the laser beam has been divided is taken as (here $n = 2400$),

$$q = \sum_n I_n(x, r) \frac{1 - e^{-K\Delta x}}{\Delta x} \quad (23)$$

where K is the inverse bremsstrahlung co-efficient (given by Kemp [4]). Bremsstrahlung radiation is the term given for the energy emitted by a charged particle as it is decelerated in the vicinity of another charged particle, where by virtue of energy conservation the loss of kinetic energy is balanced by the energy of the emitted electromagnetic radiation. In the case of inverse bremsstrahlung it is the energy input by the laser which causes an acceleration of the charged particles and thus increases the energy within the plasma. For an electron-ion interaction the inverse bremsstrahlung co-efficient can be calculated using,

$$K_{EI} = n_e n_i Q_{EI} G [\exp(h_p c / \lambda k_B T) - 1] \quad (24)$$

where Q_{EI} is electron-ion absorption cross-section. From Wang [3] this can be defined as,

$$Q_{EI} = \frac{Z^2 e^6 \lambda^3}{\mu_r 24 \epsilon_0^3 c^4 h_p \pi^2 m_e^2} \left(\frac{m_e}{6 \pi k_B T} \right)^{1/2} = 1.37 \times 10^{-27} \lambda^3 / T^{1/2} \quad (25)$$

where Z is the level of ionization of the atom (e.g. for N^+ $Z = 1$, while for N^{2+} $Z = 2$). In SI units $Q_{EI} = 1.37 \times 10^{-27} \lambda^3 / T^{1/2}$ which has units of m^5 . The term μ_r is real refractive index which is assumed equal to 1.

The variable G in Eq. 24 is the free-free Gaunt factor. For the current analysis the Gaunt factor is approximated by the following formula[5],

$$G = 1.04 + 3.74 \times 10^{-5} T - 3.28 \times 10^{-10} T^2 \quad (26)$$

Since the Gaunt factor is a function of the incident wavelength (photon energy) and the temperature it must be modified depending on the wavelength of the laser. In addition to electron-ion absorption it is also possible to have electron-neutral energy absorption which then requires,

$$K_{EN} = n_e n_i Q_{EN} [1 - \exp(-h_p c / \lambda k_B T)] \quad (27)$$

where Q_{EN} is defined as,

$$Q_{EN} = \frac{\lambda k_B^2}{h_p c} T^2 A(T) \lambda^2(A) \quad (28)$$

$A(T)$ is a curve fit based on the data from John [6] which provides the data for temperature in the range of 50 K to 25,000 K. The term $\lambda(A)$ is originally in Angstroms which after a unit conversion can be simplified to,

$$K_{EN} = 9.60 \times 10^{-5} T^2 \lambda^3 n_e n_i [1 - \exp(-h_p c / \lambda k_B T)] \quad (29)$$

The laser beam intensity term in Eq. 23 is assumed to follow a zeroth order Gaussian distribution expressed as,

$$I(x, r) = \frac{2}{\pi} \frac{P}{w^2} e^{-\frac{2r^2}{w^2}} \quad (30)$$

with the beam spot radius w as a function of the distance from the focus expressed as,

$$w = w_f \sqrt{1 + \left(\frac{\lambda(x - x_f)}{\pi w_f^2} \right)^2} \quad (31)$$

The term w_f is the finite beam waist at the focal point due to diffraction and is determined using,

$$w_f = \frac{2f\lambda}{\pi w_0} \quad (32)$$

3 Results

Simulations on several sizes of domains are considered as there is some ambiguity with regards to the size of the test chamber in Glumac and Elliot [2]. In all cases the domain is considered axisymmetric and the walls inviscid. Although there are several mechanisms responsible for the ionization of the air due to the laser, because only inverse bremsstrahlung is modelled currently the initial laser spark generation cannot be modelled (as this is primarily due to the initial release of electrons by the multi-photon effect). Therefore, for each simulation a small region of high temperature gas is initialized without any ionization, where the temperature is set so as to contain the same amount of energy deposited in the experimental setup (estimated to be 180 mJ). Outside of this region the conditions are initialized to standard atmospheric temperature and pressure.



Figure 1: Image of emission from Glumac et al. [1] at 25 ns

Figure 1 shows the extent of the initial laser spark, where it is approximately 3 mm high by 1 mm wide after 25 ns. These are the dimensions of the initial high temperature region used in the simulations, where with a total energy of 180 mJ this results in an energy density of approximately $2.6 \times 10^7 \text{ J/m}^3$. Three domain sizes are tested with dimensions as listed in Table 1.

	Small	Medium	Large
Radius [mm]	5	10	20
Length [mm]	10	20	40

Table 1: Simulation domain sizes

A comparison of the initial condition for each of the three domains is presented in Fig. 2. Each figure shows the simulation at approximately 25 ns, although due to the different grid cell sizes in each domain, for the given CFL number the actual times are slightly different. This leads to the change in the maximum temperature shown. For the large grid the time is the furthest along and thus the peak temperature shown of 14,000 K is cooler when compared to the peak seen in the small grid of 17,000 K (which is 17 ns earlier).

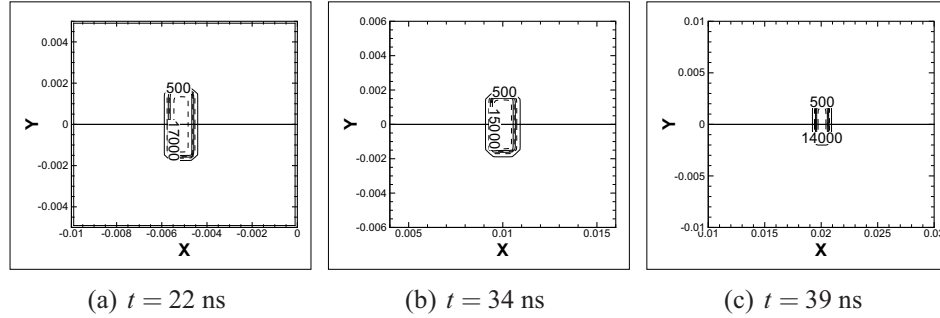


Figure 2: Initial conditions

Examining the temperature profiles at later times shows the impact the size of the domain has on the simulations. In the experimental results a toroidal shape develops as evidenced by a two lobed structure with wider plasma regions away from the axis. As shown in Fig. 3 after approximately $170 \mu s$, only the medium sized domain reproduces this result. Although the small domain also produces a toroidal structure, it does not have the characteristic wider lobes at the outer radii seen in the experimental results, while the large domain appears to show a cylindrical plasma region (the $x = 0$ axis is the axis of symmetry).

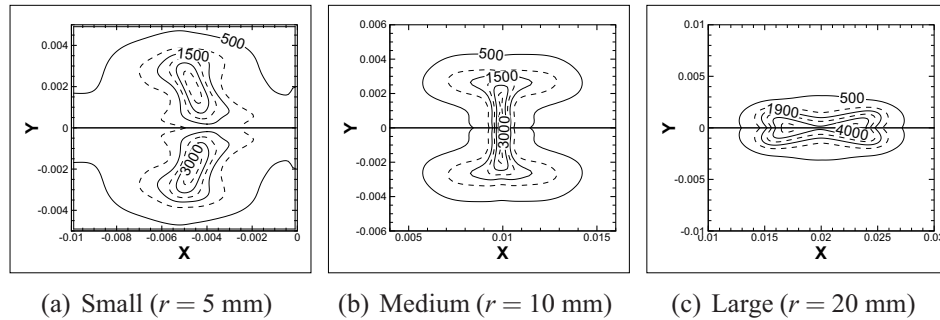


Figure 3: Temperature contours at approximately $170 \mu s$ for three domain sizes

After approximately $150 \mu s$ the experimental results show that the outer extent of the toroidal plasma region extends to a radius of approximately 3.75 mm. This is consistent with the region predicted by the medium domain where the outer contour lies between 3 and 4 mm. At approximately $500 \mu s$ the experimental plasma toroid has reached a radius

of approximately 5 mm, which is again consistent with the medium size domain results shown in Fig. 4.

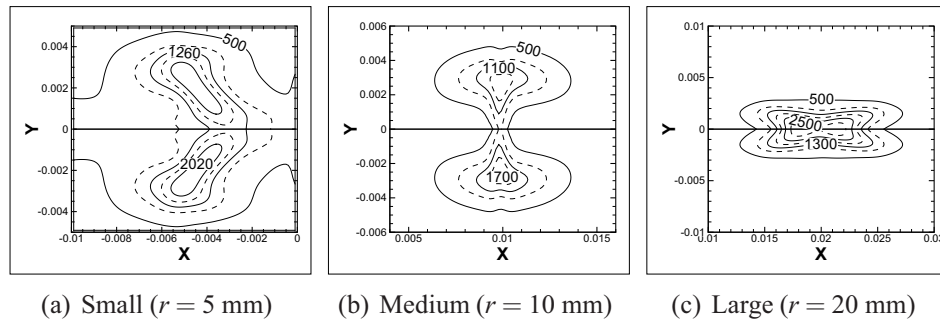


Figure 4: Temperature contours at approximately $460 \mu s$ for three domain sizes

Another feature of the flow observed experimentally is the generation of a center jet which flows in the opposite direction of the incoming laser. Although in the simulation results the initial laser energy deposition is not modelled (hence it has no direction), the streamlines shown in Fig. 5 show a definite pattern of flow being drawn inwards towards the center of the toroid. It is possible that had the initial conditions been set so as to bias the flow in a given direction to mimic the laser input direction, this inwardly drawn flow would not be symmetrical and thus flow through the toroid as observed experimentally (as opposed to meeting an equal but opposite flow as shown in Fig. 5 and thus being forced out the edges of the toroid).

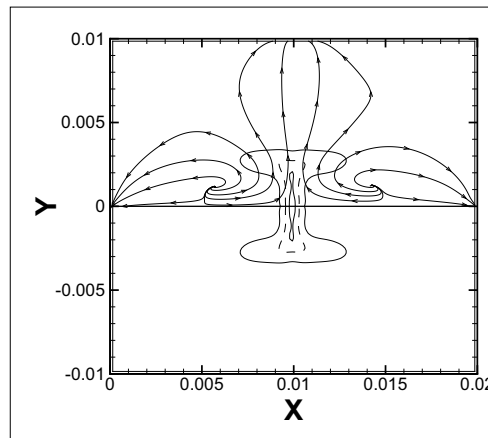


Figure 5: Streamline pattern at $170 \mu s$ obtained in the medium size domain

Despite the medium size domain's ability to qualitatively capture the experimental trends there is still a significant discrepancy in some of the quantitative results. For example, at $160 \mu s$ the maximum experimentally observed temperature has decayed to approximately

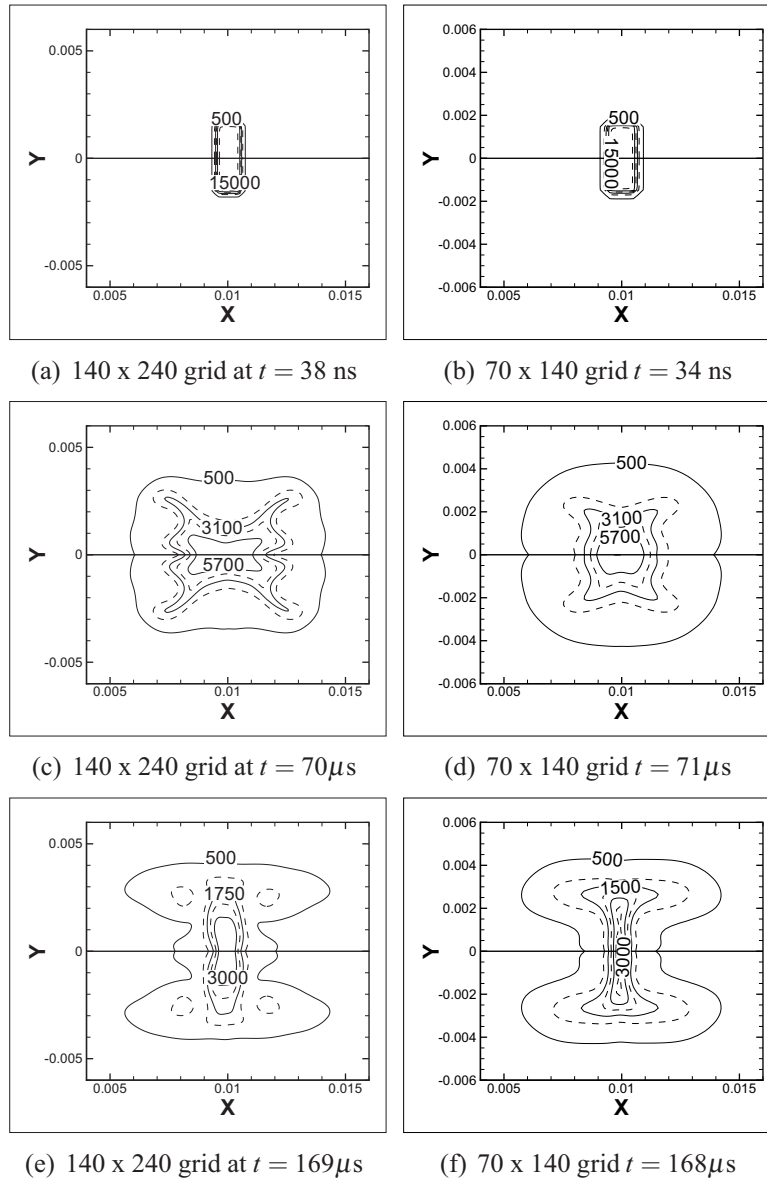


Figure 6: Comparison of temperature contours for different grid sizes in the medium sized domain

2000 K, while from Fig. 3 the medium domain still shows a maximum temperature contour of 3000 K. This discrepancy is likely due to some of the features of the code which still have not been modified to suit the Nitrogen working fluid. This includes the modelling of the emissivity, thermal conductivity, and viscosity of the working fluid which is still based on the properties of Argon.

Although the medium size domain seems to best capture the experimental results, another

simulation of the medium sized domain using approximately double the number of grid points in each direction is performed and compared against the original simulations. This comparison is shown in Fig. 6. In general the development of the plasma region is consistent between both sets of results, although there are clearly differences in the fine scale features of the flow. However, despite the influence of the grid dimensions on the dynamic flow features of the plasma development (indicating the need for a more refined grid convergence study), it is noted that the peak temperature contour in each of the simulations is approximately the same at the times shown.

This is also illustrated in Fig. 7 where the maximum temperature within the simulation is plotted versus time for all the simulations performed and compared to the experimental results of Glumac et al. [1]. Despite the fact that the dynamic flow field in each of the domain size simulation produces drastically different plasma shapes, in terms of the peak temperature decay all the simulations follow the experimental trend reasonably well. As previously mentioned, in all cases the magnitude of the maximum temperature is over-predicted by the numerical model at a given time step. A comparison of both the medium domain simulations (i.e., the coarse and fine grid results) shows that in terms of temperature decay the results follow quite closely.

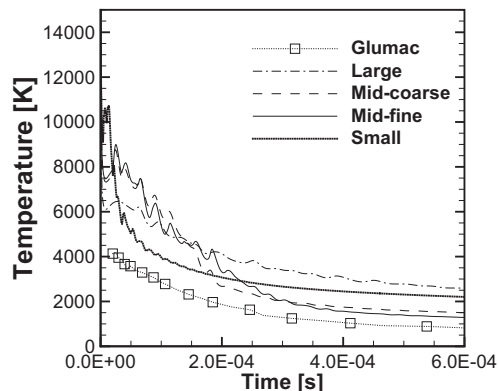


Figure 7: Maximum temperature

In all cases the temperature results at the early time steps are significantly higher than those observed experimentally, but this is due to the manner in which the simulations are initialized. In the experiments it was found that much of the temperature decay occurs over the first 50-300 ns dropping by a factor of two, with the temperature decay following an exponential trend with a time constant of approximately 87 ns. This time constant increases to approximately 410 ns for times in the micro second range.

Using the fine mesh and the medium size domain, the simulations were repeated but with the pressure reduced to 0.5 atm (the temperature was left unchanged). In this case the

results appear similar, as there is little difference seen over the time range considered. This is consistent with the experimental results where unless the pressure is reduced to values near 0.1 atm, there is little effect on the temperature decay in the micro second range. There is a slight increase in the extent of the plasma region, where for the 0.5 atm case the radius is slightly larger than 5 mm while for the 1 atm case the outer extent is slightly less than 5 mm. Although there is little effect on the temperature, a more detailed examination of the results might identify areas of larger difference.

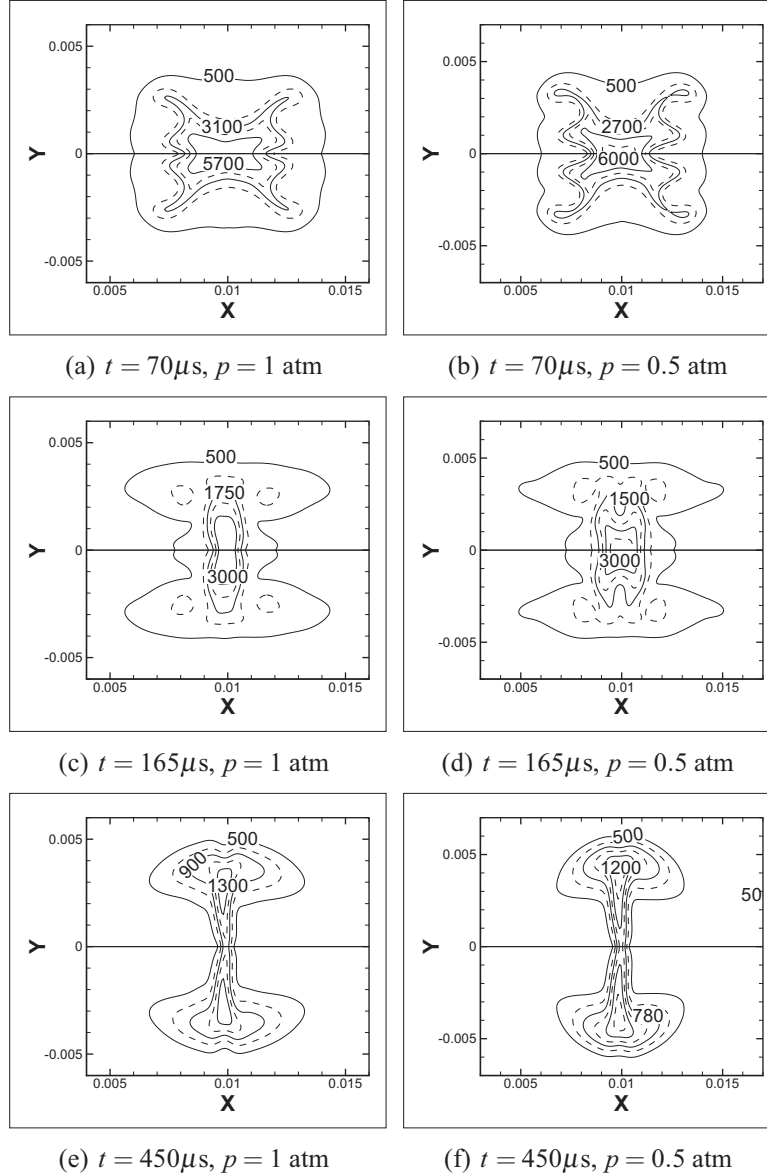


Figure 8: Comparison of temperature contours at 1 and 0.5 atm in the medium domain using the fine grid

4 Conclusions and Recommendations

Simulations of the development of a laser spark in air are performed and compared to experimental results. Many of the main features of the flow field are modelled reasonably well despite the approximations currently embedded in the numerical code. Although the laser spark generation could not be simulated, the features of the flow over the 1-500 μ s range show that the toroidal shape development can be captured as well as the center jet effect. Additionally, despite an over prediction of the exact magnitude of the plasma temperature, the qualitative temperature decay in the simulations followed that observed in the experimental data. Results are presented which show the effect of the domain size, grid dimensions, and chamber pressure on the plasma development. The effect of the chamber pressure over the range considered is small, consistent with the experimental trend. Further work is recommended with regards to examining the pressure effect on features other than simply the temperature profiles. Furthermore, since many of the significant effects of the chamber pressure are seen over the nano second range, efforts should be made to model the multi-photon mechanism of energy absorption, as well as add additional species to the simulations to allow a greater range of dissociation and ionization reactions to be considered.

Other suggestions for improving the accuracy of the numerical simulations in general are:

- Since the temperatures experienced cover a wide range from as low as 300 K to as high as 50,000 K, the dependence of the ratio of specific heats on temperature should be modelled.
- In terms of chemical composition the current code is limited to a single type of molecule and one type of ion. This works well for the noble gases such as Argon, however, for other gases the code should allow for a greater number of chemical reactions. For example, for air one could include the decomposition of both Nitrogen and Oxygen into atoms as well their ionization reactions.
- Currently the initial conditions are set to approximate the results of the initial spark development. This does not include any resulting velocities and thus effects the spatial development of the plasma region. Modelling additional energy absorption mechanisms would allow the direct modelling of the spark generation.
- The modelling of the thermodynamic properties of Nitrogen can be improved, such as the emissivity, thermal conductivity and viscosity at high temperatures. It is also recommended that the proper degeneracy levels for neutral and ionized atom/molecules be added.

References

- [1] Glumac, Nick, Elliott, Gregory, and Boguszko, Martin, Temporal and Spatial Evolution of the Thermal Structure of a Laser Spark in Air. 34rd AIAA Aerospace Sciences Meeting and Exhibit. AIAA Paper 2005-204.
- [2] Glumac, Nick and Elliott, Greg, The Effect of Ambient Pressure on Laser-Induced Plasmas in Air. 44th AIAA Aerospace Sciences Meeting and Exhibit. AIAA Paper 2006-399.
- [3] Ten-See Wang, Robert Rhodes, Thermophysics Characterization of Multiply Ionized Air Plasma Absorption of Laser Radiation. 33rd AIAA Plasmadynamics and Lasers Conference. AIAA Paper 2002-2203.
- [4] Kemp, N.H. and Lewis, P.F. (1980), Laser Heated Thruster - Interim Report, (Technical Report CR 161665) NASA.
- [5] Karzas, W.J. and Latter, R. (1961), Electron Radiative Transitions in a Coulomb Field, *Astrophysical Journal Supplement*, 6, 167–212.
- [6] John, T.L. (1975), Partition Functions and Thermodynamic Properties of Nitrogen and Oxygen Plasmas, *Monthly Notices of the Royal Astronomical Society*, 170, 5–6.

List of Acronyms and Symbols

Acronyms

CW	Continuous Wave
DBD	Dielectric Barrier Discharge
DRDC	Defence Research and Development Canada
Nd:YAG	Neodymium-doped Yttrium Aluminium Garnet

Greek Symbols

ϵ_0	Permittivity of free space
ϵ_i	Ionization energy
γ	Ratio of specific heats
κ	Laminar thermal conductivity
λ	Wavelength
μ	Laminar co-efficient of viscosity
ρ	Density
τ_{ij}	Stress

Roman Symbols

c	Speed of light
e	Electron charge
E	Total energy
f	Frequency
h_p	Plank's constant
H	Specific enthalpy
I	Laser Intensity
k_B	Boltzmann's constant
K	Inverse Bremsstrahlung co-efficient
m	Mass of a particle
MW	Molecular weight

n	Number density
p	Pressure
P	Laser power
R	Gas constant
t	Time
T	Temperature
u	x Direction velocity
v	r Direction velocity

Subscripts

axi	axisymmetric
e	electron
n	neutral
p	positive, plasma
v	viscous

This page intentionally left blank.

DOCUMENT CONTROL DATA		
(Security classification of title, body of abstract and indexing annotation must be entered when the overall document is classified)		
1. ORIGINATOR (The name and address of the organization preparing the document. Organizations for whom the document was prepared, e.g. Centre sponsoring a contractor's report, or tasking agency, are entered in section 8.)	2. SECURITY CLASSIFICATION (Overall security classification of the document including special warning terms if applicable.)	
Jason Etele, President, The Aldano Group, Inc. 5474 Edgewater Drive, Manotick, Ontario, Canada, K4M 1B4	UNCLASSIFIED (NON-CONTROLLED GOODS) DMC A REVIEW: GCEC JUNE 2010	
3. TITLE (The complete document title as indicated on the title page. Its classification should be indicated by the appropriate abbreviation (S, C or U) in parentheses after the title.)		
Report on the effect of ambient pressure on laser spark characteristics		
4. AUTHORS (last name, followed by initials – ranks, titles, etc. not to be used)		
Etele, J.		
5. DATE OF PUBLICATION (Month and year of publication of document.)	6a. NO. OF PAGES (Total containing information, including Annexes, Appendices, etc.)	6b. NO. OF REFS (Total cited in document.)
March 2012	24	6
7. DESCRIPTIVE NOTES (The category of the document, e.g. technical report, technical note or memorandum. If appropriate, enter the type of report, e.g. interim, progress, summary, annual or final. Give the inclusive dates when a specific reporting period is covered.)		
Contract Report		
8. SPONSORING ACTIVITY (The name of the department project office or laboratory sponsoring the research and development – include address.)		
Defence R&D Canada – Valcartier 2459 Pie-XI Blvd North Quebec (Quebec) G3J 1X5 Canada		
9a. PROJECT OR GRANT NO. (If appropriate, the applicable research and development project or grant number under which the document was written. Please specify whether project or grant.)	9b. CONTRACT NO. (If appropriate, the applicable number under which the document was written.)	
11az	W7701-4500907302	
10a. ORIGINATOR'S DOCUMENT NUMBER (The official document number by which the document is identified by the originating activity. This number must be unique to this document.)	10b. OTHER DOCUMENT NO(s). (Any other numbers which may be assigned this document either by the originator or by the sponsor.)	
DRDC Valcartier CR 2012-066		
11. DOCUMENT AVAILABILITY (Any limitations on further dissemination of the document, other than those imposed by security classification.)		
Unlimited		
12. DOCUMENT ANNOUNCEMENT (Any limitation to the bibliographic announcement of this document. This will normally correspond to the Document Availability (11). However, where further distribution (beyond the audience specified in (11) is possible, a wider announcement audience may be selected.)		
Unlimited		

13. **ABSTRACT** (A brief and factual summary of the document. It may also appear elsewhere in the body of the document itself. It is highly desirable that the abstract of classified documents be unclassified. Each paragraph of the abstract shall begin with an indication of the security classification of the information in the paragraph (unless the document itself is unclassified) represented as (S), (C), (R), or (U). It is not necessary to include here abstracts in both official languages unless the text is bilingual.)

14. **KEYWORDS, DESCRIPTORS or IDENTIFIERS** (Technically meaningful terms or short phrases that characterize a document and could be helpful in cataloguing the document. They should be selected so that no security classification is required. Identifiers, such as equipment model designation, trade name, military project code name, geographic location may also be included. If possible keywords should be selected from a published thesaurus, e.g. Thesaurus of Engineering and Scientific Terms (TEST) and that thesaurus identified. If it is not possible to select indexing terms which are Unclassified, the classification of each should be indicated as with the title.)

Plasma modeling; laser-based plasma

Defence R&D Canada

Canada's Leader in Defence
and National Security
Science and Technology

R & D pour la défense Canada

Chef de file au Canada en matière
De science et de technologie pour
la défense et la sécurité nationale



www.drdc-rddc.gc.ca

